Unraveling Heat Transport and Dissipation in Suspended MoSe₂ from Bulk to Monolayer

David Saleta Reig, Sebin Varghese, Roberta Farris, Alexander Block, Jake D. Mehew, Olle Hellman, Paweł Woźniak, Marianna Sledzinska, Alexandros El Sachat, Emigdio Chávez-Ángel, Sergio O. Valenzuela, Niek F. van Hulst, Pablo Ordejón, Zeila Zanolli, Clivia M. Sotomayor Torres, Matthieu J. Verstraete, and Klaas-Jan Tielrooij*

Understanding heat flow in layered transition metal dichalcogenide (TMD) crystals is crucial for applications exploiting these materials. Despite significant efforts, several basic thermal transport properties of TMDs are currently not well understood, in particular how transport is affected by material thickness and the material's environment. This combined experimental–theoretical study establishes a unifying physical picture of the intrinsic lattice thermal conductivity of the representative TMD MoSe₂. Thermal conductivity measurements using Raman thermometry on a large set of clean, crystalline, suspended crystals with systematically varied thickness are combined with ab initio simulations with phonons at finite temperature. The results show that phonon dispersions and lifetimes change strongly with thickness, yet the thinnest TMD films exhibit an in-plane thermal conductivity that is only marginally smaller than that of bulk crystals. This is the result of compensating phonon contributions, in particular heat-carrying modes around ≈0.1 THz in (sub)nanometer thin films, with a surprisingly long mean free path of several micrometers. This behavior arises directly from the layered nature of the material. Furthermore, out-of-plane heat dissipation to air molecules is remarkably efficient, in particular for the thinnest crystals, increasing the apparent thermal conductivity of monolayer MoSe₂ by an order of magnitude. These results are crucial for the design of (flexible) TMD-based (opto-) electronic applications.

1. Introduction

2D materials in single or few-layer form have great potential as nanometer thin building blocks for flexible and wearable (opto-)electronic and photonic devices.[1–3] Concrete examples of promising devices based on 2D semiconducting transition metal dichalcogenides (TMDs) are photodetectors,[4,5] transistors,[6,7] gas sensors,[8,9] and thermoelectric generators.[10] Many of these applications rely on the remarkable properties of van der Waals crystals that appear upon reaching, or approaching, the monolayer thickness limit. Examples are the crossover from indirect to direct bandgap at the monolayer limit of MoS₂ and other TMDs,[11] a metal-to-semiconductor transition in PtSe₂,[12] mechanical softening of MoSe₂ films,[13] and layer-dependent magnetic phases in CrI₃.[14] The ability to control the thickness of layered materials allows one to engineer their electrical, optical, mechanical, and magnetic properties.

The thermal properties of layered materials have so far received less attention

D. Saleta Reig, S. Varghese, R. Farris, A. Block, J. D. Mehew,
M. Sledzinska, A. El Sachat, E. Chávez-Ángel, S. O. Valenzuela,
P. Ordejón, C. M. Sotomayor Torres, K.-J. Tielrooij
Catalan Institute of Nanoscience and Nanotechnology (ICN2)
BIST and CSIC
Campus UAB, Bellaterra (Barcelona) 08193, Spain
E-mail: klaas.tielrooij@icn2.cat

O. Hellman
Dept of Molecular Chemistry and Materials Science
Weizmann Institute of Science
Rehovoth 76100, Israel

The ORCID identification number(s) for the author(s) of this article
can be found under https://doi.org/10.1002/adma.202108352.

P. Woźniak, N. F. van Hulst
ICFO-Institut de Ciéncies Fotóniques
Mediterranean Technology Park, Castelldefels
Barcelona 08860, Spain

S. O. Valenzuela, N. F. van Hulst, C. M. Sotomayor Torres
ICREA
Pg. Lluís Companys 23, Barcelona 08010, Spain

Z. Zanolli
Chemistry Department and ETSF
Debye Institute for Nanomaterials Science
Utrecht University
the Netherlands

M. J. Verstraete
Nanomat, Q-Mat, CESAM, and European Theoretical Spectroscopy Facility
Université de Liége
Liége B-4000, Belgium

**ADVANCED
SCIENCE NEWS**

www.advancedsciencenews.com

**ADVANCED
MATERIALS**

www.advmat.de

than their electronic and optical counterparts, although several remarkable and exotic thermal transport phenomena have been found. Interesting observations are the ultrahigh in-plane thermal conductivity of graphene[15] and hexagonal boron nitride (hBN),[16] the highly anisotropic thermal conductivity of TMDs[17] and stacked TMD films,[18] and the occurrence of second sound in graphite.[19] However, there are still many open questions concerning the very basic, yet critical, thermal transport properties of TMDs at room temperature.[20] In particular, experimental values of the in-plane lattice thermal conductivity κ vary substantially, ranging from 6[21] to 59 W m^{-1} K^{-1} [22] for MoSe$_2$, and it is not clear how the thermal conductivity changes with the thickness of TMD flakes.[20,23–25] A systematic experimental study with a broad range of thicknesses is lacking. Moreover, the calculated thermal conductivities extracted from atomistic simulations also give scattered results, ranging from 17.6[26] to 54 W m^{-1} K^{-1} [27] for monolayer MoSe$_2$. Also in the theoretical approaches, a systematic thickness variation is lacking, as most studies focused either on monolayer or bulk MoSe$_2$. The effect of the environment on thermal transport in TMDs has furthermore not received much attention, despite that a significant effect was observed for graphene.[28] This situation for MoSe$_2$ is representative for all layered materials in the TMD family,[20] and indicates that a proper physical understanding of thermal transport in TMDs—and in particular the effect of material thickness and environment in the limit toward monolayer—is missing.

Performing reliable experimental and theoretical thermal transport studies over a broad thickness range, down to the molecular monolayer, is challenging. Experimental approaches can be susceptible to thickness-dependent artifacts, and require reproducible fabrication of a large number of clean samples with controlled thicknesses. Theoretical approaches based on molecular dynamics simulations are limited in accuracy by the choice of empirical interatomic potentials, while ab initio simulations often examine phonons at 0 K, rather than at finite temperature. Simulations of thicknesses other than monolayer and bulk are computationally costly, and therefore so far non-existent, with the only exceptions being an ab initio study on MoS$_2$ as a function of thickness limited to the range 1–3 layers[29] and a molecular dynamics study on monolayer and bilayer MoS$_2$.[30]

In this work, we overcome these technical challenges, which enables us to develop a deep understanding of thermal transport properties of TMD crystals. In particular, we establish how the in-plane lattice thermal conductivity κ depends on crystal thickness, that is, the number of molecular layers. For this, we systematically vary the thickness down to the monolayer limit, both in experiment and simulations. Whereas we focus on MoSe$_2$ crystals, the obtained results are representative for other TMDs. In our experimental approach, we exploit the widely used technique of Raman thermometry, where we carefully identified and eliminated important artifacts, such that we obtain the intrinsic thermal conductivity. In our theoretical approach, we perform ab initio simulations based on density functional theory (DFT) and Boltzmann transport theory, including anharmonic renormalization yielding accurate results also at finite temperature. We employ SIESTA,[31,32] which is particularly suitable for atomistic simulations with a large number of atoms, such that we can obtain results up to several molecular layers.

We find that the main contribution to the in-plane thermal conductivity in few-layer MoSe$_2$ comes from phonon modes centered around 1 THz. Toward the monolayer limit, the contribution of these modes decreases substantially, as there are fewer modes and the phonon lifetimes decrease. These effects are counteracted by the appearance of "surface" modes around ≈0.1 THz with an exceptionally long mean free path (MFP) of several micrometers, which contribute substantially to thermal transport. This results in an in-plane thermal conductivity that progressively increases from a value of $\kappa \approx$20 W m^{-1} K^{-1} for the thinnest films, toward ≈32 W m^{-1} K^{-1} for the thickest films, at a temperature of ≈400 K. This behavior originates from the layered nature of 2D-bonded MoSe$_2$ and similar TMDs, and is different from the behavior of nonlayered materials, such as 3D-bonded silicon. In such materials, the thermal conductivity keeps decreasing for thinner films, due to increased boundary scattering at the surfaces.[33] We note that it has so far not been possible to experimentally produce such materials with a thickness below a nanometer and a lateral size of several microns, such as our MoSe$_2$ films.

Finally, we find that thermal transport in MoSe$_2$ is strongly affected by the material's environment, in particular for monolayer crystals, where >80% of the thermal power is lost through out-of-plane heat dissipation to surrounding air molecules. We extract a remarkably large heat transfer coefficient h_c up to ≈50 000 W m^{-2} K^{-1} for monolayer MoSe$_2$, and an apparent thermal conductivity above 250 W m^{-1} K^{-1}. This is larger than the 140 W m^{-1} K^{-1} of bulk crystalline silicon.[33] These results highlight the highly promising applicability of TMDs in (opto)electronic applications, where material thicknesses of a few nanometers, or less, are required.

2. Results and Discussion

2.1. Experimental Results

One of the most common methods to study thermal properties of thin films is Raman thermometry,[22–25] where a laser beam serves both as a heater and a thermometer. The thermometer works via Raman scattering of the laser light, where the frequency shift of a temperature-calibrated Raman mode serves as a probe of the local temperature of a suspended sample. This technique benefits from a relatively simple implementation, contactless nature, and no stringent sample requirements, apart from the presence of a temperature-sensitive Raman active mode. In our experiments (see Experimental Section for details), we use continuous wave (CW) light with a wavelength of 532 nm to heat a local spot with a $1/e$ spot size r_0 of ≈1 µm in the center of a suspended MoSe$_2$ crystal (see **Figure 1**a,b). Subsequent cooling occurs—in the ideal situation—by radial, diffusive flow of heat toward the edge of the suspended region of the crystal, where the substrate acts as a heat sink. We probe the temperature at the location of the laser spot, corresponding to the steady-state situation where laser-induced heating is compensated by cooling through heat flow and subsequent heat sinking. Thus, a higher (lower) steady-state temperature
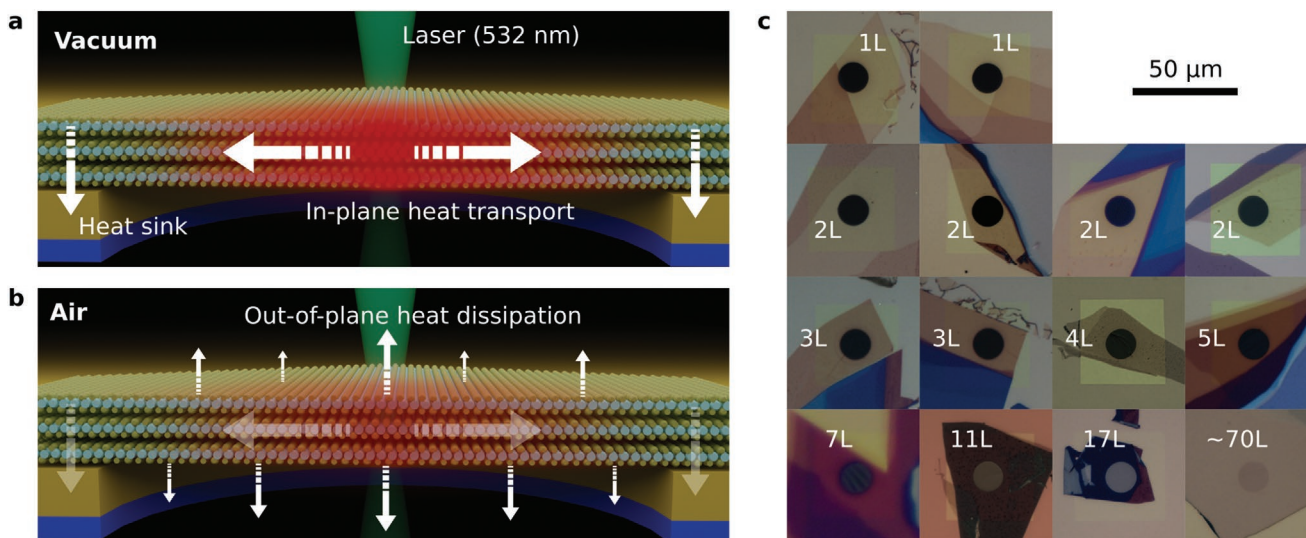
**ADVANCED
SCIENCE NEWS**

www.advancedsciencenews.com

**ADVANCED
MATERIALS**

www.advmat.de

Figure 1. Concept of the thermal transport experiments and investigated samples. a) Schematic representation of a suspended trilayer MoSe$_2$ crystal in vacuum, where absorbed 532 nm laser light in the center of the suspended region leads to local heating, and subsequent heat spreading toward the heat sink at the edge of the suspended region, establishing a steady state temperature profile that depends on the in-plane thermal conductivity κ. b) In air, additional out-of-plane dissipation occurs. c) Optical reflection images of suspended MoSe$_2$ flakes with a thickness varying from monolayer to ≈70 layers, suspended over gold-coated substrates with circular holes with a radius of 7.5 μm (black/grey central circle), inside 200 nm thick Si$_3$N$_4$ membranes (yellow squares). Several flakes have regions with different thicknesses, yet the thickness is uniform in the suspended region in all cases.

indicates less (more) efficient cooling, which in turn implies a lower (higher) κ. For thin exfoliated TMD flakes with high crystallinity the obtained κ corresponds to in-plane transport, as the out-of-plane thermal conductivity is typically more than an order of magnitude lower.[17]

We use exfoliated MoSe$_2$ crystals suspended over substrates with a circular hole, fabricated using dry transfer, as described in the Methods. This fabrication method leads to single-crystalline, residue-free crystals, with an unprecedentedly large suspended area of 177 μm^2,[34] allowing us to probe the intrinsic material properties of MoSe$_2$ crystals. We systematically vary the thickness from monolayer (1L) up to ≈70 layers (70L), fully covering the 1L to 5L range (see Figure 1c). This corresponds to a thickness ranging from 0.7 nm up to ≈50 nm. We carefully determined these thicknesses using a combination of optical contrast, atomic force microscopy and photoluminescence measurements (see Figure S1, Supporting Information). Importantly, we use more than one sample with the same thickness in the 1L to 3L regime—including two monolayer, four bilayer and two trilayer samples—in order to assess the reproducibility of both our samples and our experimental technique. We suspend the flakes over circular holes with a radius of 7.5 μm, in the center of 200 nm thick Si$_3$N$_4$ membranes that are coated with a 50 nm thick layer of gold (see Figure 1c). Gold coating facilitates sample fabrication,[34] and importantly ensures efficient heat sinking to the substrate. We also studied other monolayer samples suspended over smaller holes (2.5 and 5 μm), and flakes with varying thickness, transferred on Si$_3$N$_4$ substrates without gold coating, aimed at understanding and eliminating possible artifacts affecting the extracted thermal conductivity (see Figures S5 and S6, Supporting Information).

We perform Raman thermometry measurements on all the suspended MoSe$_2$ samples shown in Figure 1c, exploiting the temperature-sensitive A_{1g} Raman mode (see **Figure 2**). In Figure 2b, we show how the peak frequency of this mode shifts with laser power at the sample position, P, for monolayer MoSe$_2$ (see Figure S2, Supporting Information for the results for other thicknesses): a higher laser power induces a larger temperature increase ΔT, and therefore a larger red-shift. We correlate the red-shift of the A_{1g} peak, $\Delta \nu$, with the increase in temperature, ΔT, by measuring the Raman spectrum at very low incident power, while varying the temperature of the crystal using a controlled sample stage (see Figure 2c for monolayer MoSe$_2$, and Figure S3, Supporting Information for the results for other thicknesses). We find that the temperature coefficients $\chi_T = \partial \nu / \partial T$ change from −0.007 cm^{-1} K^{-1} for bulk to −0.015 cm^{-1} K^{-1} for monolayer MoSe$_2$ (see Table S1, Supporting Information). We then use these temperature coefficients to convert the laser-induced red-shift $\Delta \nu$ of the peak of the Raman signal into a local temperature rise that depends on laser power $\Delta T(P)$.

In order to extract the in-plane thermal conductivity, we perform a linear fit to the extracted ΔT as a function of absorbed laser power P_{abs}, obtaining the slope $\partial T / \partial P_{abs}$, and then use the following equation[35]

$$\kappa = \alpha \cdot \frac{1}{2\pi d} \cdot \left(\frac{\partial T}{\partial P_{abs}} \right)^{-1} \cdot \ln\left(\frac{R}{r_0} \right) \tag{1}$$

where R is the hole radius, r_0 is the laser spot radius, d is flake thickness, and α is a prefactor that is a function of the ratio R/r_0. For our experimental conditions, $\alpha \approx 1$.[35] Equation (1) for κ is valid when the only cooling channel is in-plane diffusive heat transport to the edge of a circular suspended material, where perfect heat-sinking occurs, such that the crystal is at ambient temperature. The accurate extraction of κ relies on knowledge of the laser spot size r_0 and the optical absorption of each of the
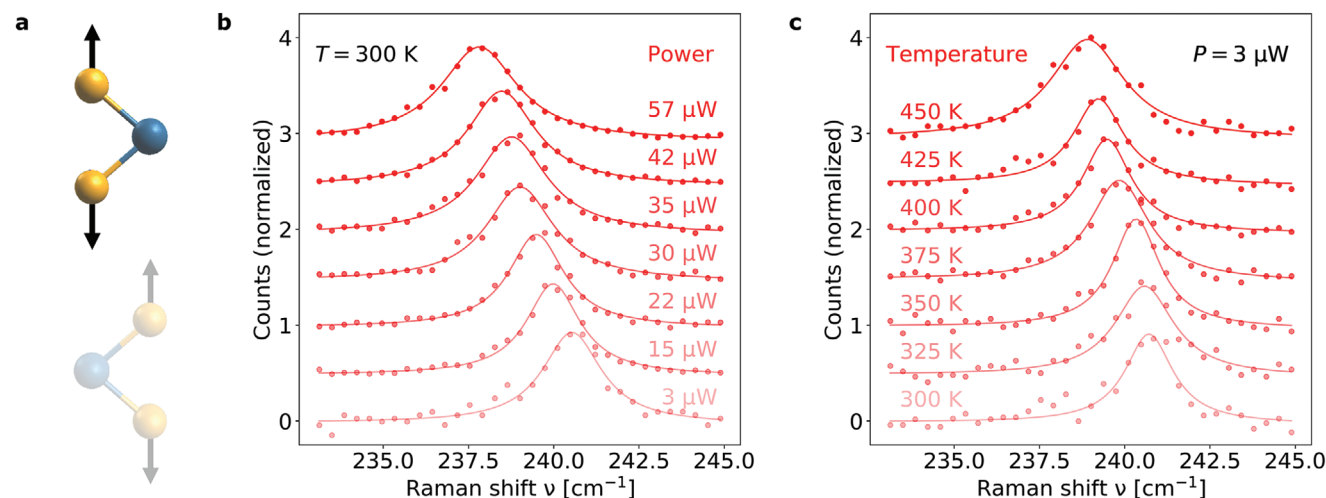
**ADVANCED
SCIENCE NEWS**

www.advancedsciencenews.com

**ADVANCED
MATERIALS**

www.advmat.de

Figure 2. Raman thermometry of a suspended monolayer MoSe$_2$. a) Schematic representation of the A$_{1g}$ mode of MoSe$_2$. b) Raman spectra at 532 nm for increasing laser power P, showing an increasing red-shift of the A$_{1g}$ mode due to laser-induced heating. c) Calibration measurements of Raman spectra at 532 nm for increasing sample temperature of the sample stage, showing an increasing red-shift. Here, the laser power was kept very low, in order to avoid laser-induced heating. For similar measurements on thicker flakes, see Figures S2 and S3, Supporting Information.

flakes, which were measured independently (see Experimental Section). We confirmed the validity of Equation (1) using a numerical simulation of the Raman thermometry experiment (see Figure S4, Supporting Information). Importantly, this numerical model allows for including additional physical processes, such as out-of-plane heat dissipation.

Before presenting the results, we point out the importance of eliminating artifacts that can occur in Raman thermometry measurements on such ultrathin samples, in particular related to the substrate and environmental conditions (see Item S6, Supporting Information). After considering several substrate designs, we concluded that using gold-coated substrates with a hole radius of 7.5 μm leads to the elimination of several important artifacts, as illustrated in Figure S5e, Supporting Information. We thus study the effect of crystal thickness on the thermal

conductivity using our experimental approach of Raman thermometry, crucially performing these measurements under vacuum conditions (see **Figure 3**). We plot ΔT as a function of absorbed power P_{abs} (Figure 3a), and observe a clear trend with the thickness of the samples: thinner crystals heat up more significantly for the same absorbed power. This is intuitive, as thinner crystals have a smaller volume in which the same amount of heat is deposited, and thus a smaller thermal capacitance. Plotting $\Delta T \cdot d$ as a function of P_{abs} (Figure 3b) gives a slope that is directly representative of the thermal conductivity κ (see Equation (1)). We now see that all data points fall on almost the same slope, suggesting that the intrinsic thermal properties of MoSe$_2$ are not dramatically affected by crystal thickness.

A quantitative analysis of the experimental data using Equation (1) results in a weakly decreasing thermal conductivity
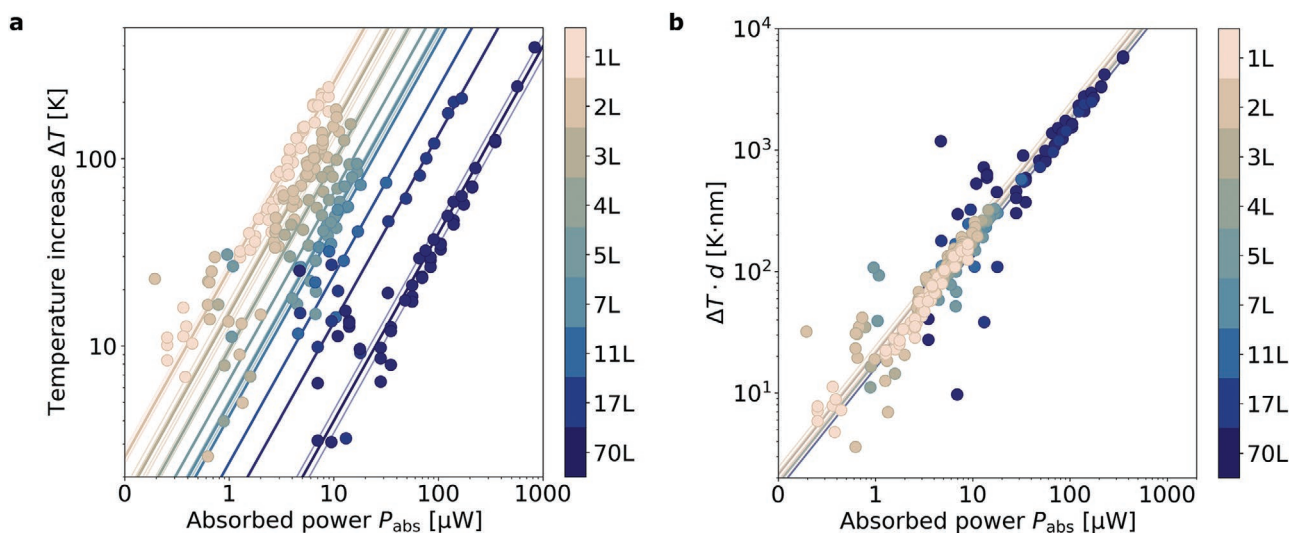

Figure 3. Raman thermometry of MoSe$_2$ as a function of crystal thickness. a) Temperature rise ΔT as a function of absorbed power P_{abs} for MoSe$_2$ crystals of varying thickness. b) The same data as in (a), now multiplied by the thickness of each crystal, such that the slope is representative of κ. Each layer thickness has its own corresponding color (see color bars). Solid lines are linear fits to the data.

**ADVANCED
SCIENCE NEWS**

www.advancedsciencenews.com
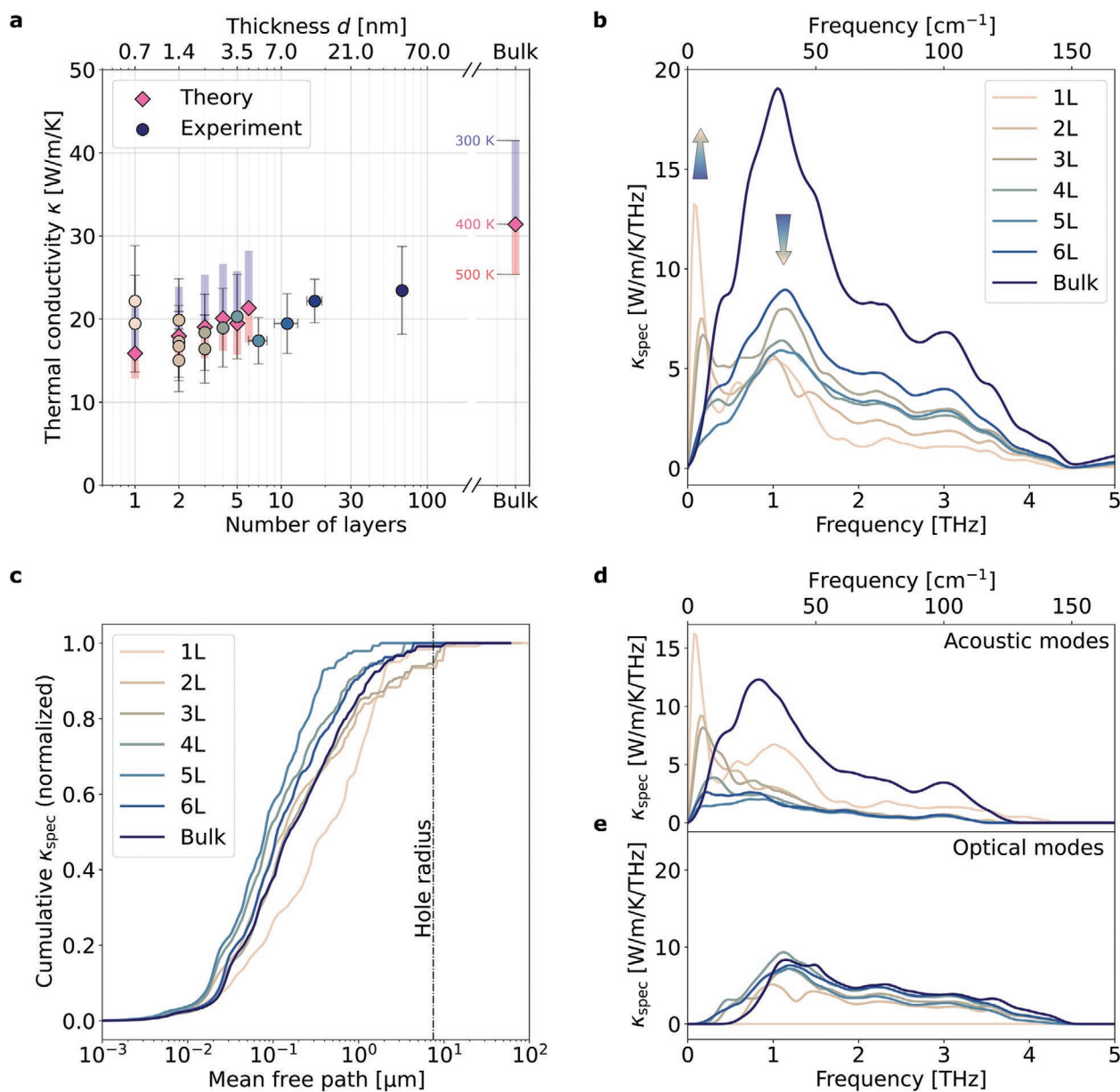
**ADVANCED
MATERIALS**

www.advmat.de

Figure 4. Microscopic understanding of heat transport in MoSe₂. a) In-plane thermal conductivity of MoSe$_2$ crystals as a function of thickness, using our experimental (circles) and theoretical (diamonds) approach. The experimental error bars represent the 70% confidence interval, while the theoretical conductivities show how the values vary between a temperature of 300 and 500 K. b) Spectrally decomposed thermal conductivity κ_{spec} as a function of phonon frequency, indicating how toward thinner films an increasing contribution from a sub-THz mode compensates the decreasing contribution from modes around 1 THz. c) Decomposed in-plane thermal conductivity as a function of phonon MFP. The cumulative thermal conductivity is normalized by the overall in-plane thermal conductivity. d,e) Spectrally decomposed thermal conductivity κ_{spec} for d) acoustic-like modes and e) optical-like modes.

for crystals with a thickness of 70L down to monolayer, (see **Figure 4**a). In the Figure S8, Supporting Information, we compare our values for the in-plane thermal conductivity with the available experimental results in the literature.[17,21,22,36] Most strikingly, our systematic thickness variation demonstrates a relatively weak effect of crystal thickness. The thermal conductivity is smaller for the thinnest samples than for the thickest sample (70L), whereas some experimental literature values suggest the opposite trend (see Figure S8, Supporting Information). We ascribe this discrepancy to the fact that not

all measurements in the literature were performed under the same conditions nor with similar substrates, and often using noncoated substrates with rather small hole sizes, which can all lead to an overestimation of the thermal conductivity, in particular for monolayer samples. Besides, if any contamination would be present on a monolayer sample, this could also act as a thermal dissipation channel, giving rise to an increased apparent thermal conductivity. In our case we used artifact-minimized substrates and well-characterized, clean samples, as shown in ref. [34].

**ADVANCED
SCIENCE NEWS**

www.advancedsciencenews.com

**ADVANCED
MATERIALS**

www.advmat.de

2.2. Theoretical Results and Discussion of Thickness Effect

In order to interpret and understand our experimental results, we compute the thermal properties of $MoSe_2$ using density functional theory, as implemented in SIESTA,[32] in combination with the temperature-dependent effective potential (TDEP) method that allows to take into account phonons at a nonzero temperature.[37,38] In brief (see Experimental Section for details), with this method we identify harmonic and anharmonic interatomic force constants taking into account atomic displacements and forces of a canonical ensemble at a given temperature. These computed force constants are the representation of the thermally averaged Born–Oppenheimer potential energy surface of the atomic displacements around the equilibrium positions. With this method we compute the phonon dispersion (see Figure S9, Supporting Information) and the anharmonic terms of the interatomic potential, in order to obtain the in-plane lattice thermal conductivity κ. We compute κ for bulk $MoSe_2$, and for 2D crystals with thicknesses from 6L down to the monolayer and between 300 and 500 K.

We compare the theoretically obtained in-plane thermal conductivity of $MoSe_2$ crystals with different thicknesses to the experimental results (see Figure 4a). For the thinnest crystals, we see that the first-principles-based results at 400 K show a κ of 15 W m^{-1} K^{-1}, weakly increasing to 21 W m^{-1} K^{-1} for 6L, and then increasing further to 32 W m^{-1} K^{-1} for bulk. The experimental values similarly increase from a value below 20 W m^{-1} K^{-1} for bilayer sample, to a value above 20 W m^{-1} K^{-1} for 17L and 70L. Considering the experimental uncertainty and the temperature range of the theoretical results, the results are in quantitative agreement. Importantly, both results show that there is a weak effect of crystal thickness on the thermal conductivity. Furthermore, if there is any effect, it is opposite to the effect in graphite, which shows an increase in thermal conductivity upon decreasing crystal thickness, with monolayer graphene exhibiting the largest thermal conductivity.[15,39] In Figure S10, Supporting Information, we compare our values for the in-plane thermal conductivity with the available results in the literature.[26,27,40,41] Moreover, we performed the same simulations for the TMD materials WSe_2 and MoS_2, which show a similar trend (see Figure S12, Supporting Information). This suggests that the trend we observe both experimentally and theoretically is representative of the broader family of TMD materials.

Our simulation results provide important physical insights for the observed weak effect of crystal thickness on κ for TMDs: we examine which phonons contribute to the total thermal conductivity by plotting the spectrally decomposed thermal conductivity of $MoSe_2$ κ_{spec} (see Figure 4b). We find that for bulk crystals, the largest contribution comes from modes around 1 THz. This contribution gradually decreases with the crystal thickness. However, toward the monolayer limit, modes with a frequency well below 1 THz start playing an important role. We confirm this picture by examining the phonon mean free path of each of the phonon modes in the decomposed thermal conductivity (see Figure S14, Supporting Information). We show the cumulative thermal conductivity as a function of MFP (see Figure 4c), and observe that in the monolayer case, an increased fraction of the conductivity is carried by low-frequency modes with a relatively long MFP. This result also highlights the importance of using large hole sizes, as a significant fraction of κ is carried by phonons with a MFP of several microns, which confirms that our experimental hole size is not significantly affecting the extracted κ through edge scattering: phonons with a MFP <7.5 μm contribute to >90% of the total thermal conductivity.

In order to gain more understanding of the key phonon modes, we decompose the spectral contribution into acoustic modes (see Figure 4d) and low-frequency optical modes (see Figure 4e). For the latter, we only take into account modes below 4 THz: the thermal conductivity of higher optical modes is negligible. The contribution of the optical modes, which are centered slightly above 1 THz and have an interlayer character, weakly decreases with decreasing crystal thickness. The acoustic contribution that is centered below 1 THz exhibits stronger thickness effects, with the most striking effect being the increasingly strong contribution of the flexural mode situated at ≈0.1 THz for thin $MoSe_2$. Thus, from the simulation results in Figure 4b–e we understand that toward the monolayer limit, the decreasing contribution to κ from modes around 1 THz is rather effectively compensated by the increasing contribution of modes with a much lower frequency, in particular a low-energy flexural mode, thus resulting in an overall weak effect of material thickness.

This is a surprising result, because both the phonon dispersions and the phonon lifetimes (see Figure S13, Supporting Information) change drastically with thickness, as is also clear from the spectrally decomposed thermal conductivity in Figure 4. Moreover, it is remarkable that significant amounts of heat are carried by modes with a mean free path of several micrometers inside a material with sub-nanometer thickness. This shows that out-of-plane boundary scattering does not play any role for the in-plane thermal conductivity of 2D van der Waals bonded TMDs. This is in large contrast with thin films of 3D bonded materials, where the thermal conductivity is typically thought to be limited by boundary scattering at the film surface, limiting the mean free path out of plane to an effective scattering thickness. For 2D materials this is not the case: the very long lifetimes of low energy modes in thin $MoSe_2$ are made possible by the weakness of the van der Waals interlayer scattering, which is generic for all 2D materials, and leads to the well-known thermal transport anisotropy of an order of magnitude.[17] One intuitive way of understanding the difference between thermal transport in 3D- and 2D-bonded materials is that the latter already contains "internal" surfaces, between adjacent layers. Thus, for increasingly thin films, non-layered materials experience surface scattering that is increasingly more frequent, whereas in layered materials modes that would undergo surface scattering are—to some extent—already impeded by the "internal" surfaces between different layers. In our theoretical simulations, the full physical thickness is taken into account: surface vibrations are distinguished explicitly, and the scattering between bulk-localized and surface-localized modes is included in the anharmonic three-phonon interatomic force constants. The simulated surface does not contain additional sources of scattering (strain, residues, defects, etc.) which would also limit the mean free path. The agreement with experiments is a further confirmation of the very clean and ideal nature of the experimental samples.
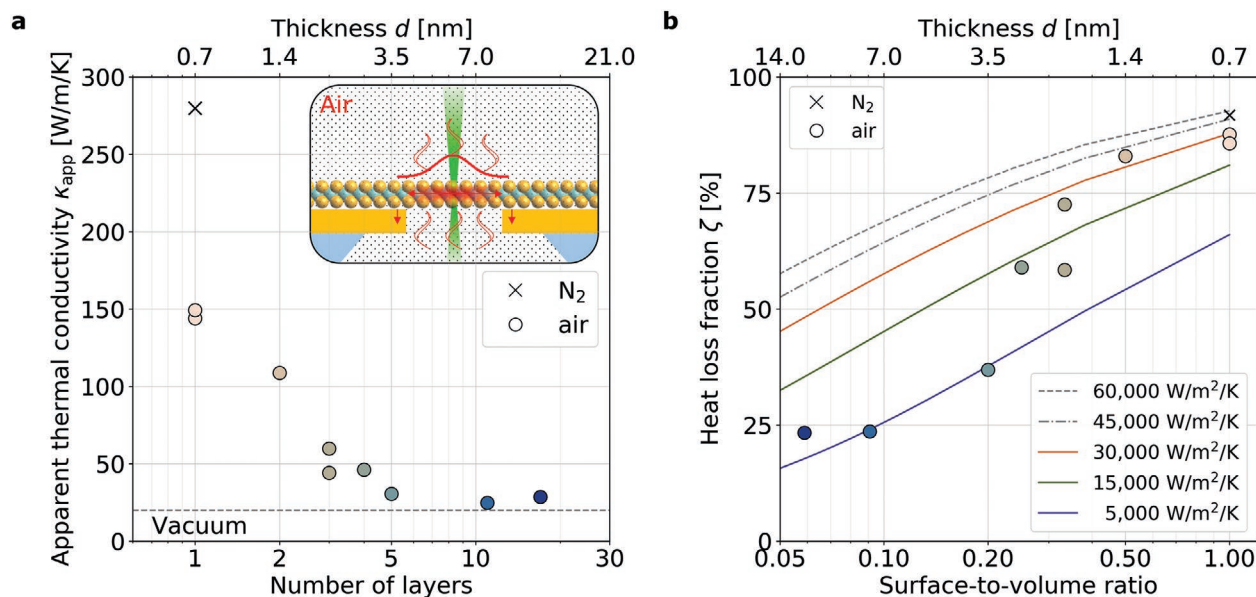
**ADVANCED
SCIENCE NEWS**

www.advancedsciencenews.com

**ADVANCED
MATERIALS**

www.advmat.de

Figure 5. Air-mediated losses in suspended MoSe$_2$. a) Apparent in-plane thermal conductivity of suspended MoSe$_2$ flakes on large, gold-coated holes as measured in air and nitrogen environments. b) Relative power losses to air, extracted by comparing measurements performed in vacuum with those performed in air. Solid lines represent the simulated power losses for different heat transfer coefficients (see Experimental Section).

2.3. Out-of-Plane Dissipation to the Environment

Many properties of thin, layered materials have been shown to be sensitive to the environment.[30] In the case of thermal properties, a relatively small effect caused by heat transport to gas molecules was observed for suspended graphene.[28] We examine the effect of the surrounding environment on thermal transport in our MoSe$_2$ crystals, by performing Raman thermometry experiments both in vacuum and in air, for several samples with different thicknesses. In **Figure 5**a, we show the obtained apparent thermal conductivity κ_{app} as a function of flake thickness in the case of air, instead of vacuum. We find a thermal conductivity that is slightly higher in air than in vacuum for thick flakes, whereas it is almost an order of magnitude higher for monolayer MoSe$_2$. We repeated this experiment with a monolayer sample in nitrogen atmosphere, and found an even larger apparent thermal conductivity. The reason for this large effect is likely that the presence of air or nitrogen introduces an additional cooling channel. In addition to in-plane diffusion from the hot spot to the heat sink, heat dissipation occurs by transfer to the ambient molecules as a sink (schematically depicted in the inset of Figure 5a). The relative effect of this competing dissipation channel is much larger than in the case of graphene, because the in-plane thermal conductivity of monolayer MoSe$_2$ is much smaller than that of graphene. We note that Equation (1) is not valid if there is an additional cooling channel, which means that the obtained apparent thermal conductivity κ_{app} in air is not an intrinsic material property of MoSe$_2$. However, it can be seen as an effective parameter describing heat transport in the combined air-MoSe$_2$ system. Thus, the obtained thermal conductivity above 250 W m^{-1} K^{-1}, which is larger than the 140 W m^{-1} K^{-1} of bulk crystalline silicon[33] is a promising result.

In order to understand the observed effect of the environment in more detail, we include additional cooling channels in our simulation of the Raman thermometry experiment (see Equation (S1), Supporting Information). We first consider radiative cooling, estimating its maximum possible contribution by using a ΔT of 200 K, which is the largest value we used in our experiment (see Figure 3a). The results are shown in Supporting Information, and indicate a negligible effect of <0.1% for radiative cooling at such temperatures. Due to the T^4-scaling, this cooling channel will likely only start playing a role at significantly higher temperatures ($\Delta T \gg 200$ K). The next cooling channel we consider is that of out-of-plane heat dissipation from MoSe$_2$ to the surrounding air molecules. We plot the experimentally obtained loss fraction, defined as $\zeta = 1 - \kappa_{vac}/\kappa_{app,\ air}$, as a function of surface-to-volume ratio of the crystal (see Figure 5b), and compare it to our simulation of the Raman thermometry experiment that includes an out-of-plane heat transfer term. We find a heat loss fraction ζ of ≈20% for the lowest surface-to-volume ratio, which we can reproduce with a heat transfer coefficient h_c of ≈5000 W m^{-2} K^{-1}. For monolayer MoSe$_2$ in air, on the other hand, we find >80% loss, which we can reproduce with a h_c of ≈30 000 W m^{-2} K^{-1}. For the monolayer in nitrogen environment, we estimate a slightly larger heat transfer coefficient of ≈50 000 W m^{-2} K^{-1}. These are much larger values than the typical values for the convective heat transfer coefficient found in the literature,[22,23] even for forced convection by gases: $h_c = 25 - 250$ W m^{-2} K^{-1}.[42] Our value, however, is very close to the value observed for monolayer graphene (2.9×10^4 W m^{-2} K^{-1}),[28] and close to the ideal heat transfer coefficient to air at ambient pressure and temperature with an ideal molecular accommodation coefficient (10^5 W m^{-2} K^{-1}).[28] The larger heat transfer coefficient for nitrogen, compared to air, could be related to the lower humidity. Importantly, these results provide clear evidence that

**ADVANCED
SCIENCE NEWS**

www.advancedsciencenews.com

**ADVANCED
MATERIALS**

www.advmat.de

out-of-plane heat dissipation to air plays an important role in the cooling dynamics of suspended ultrathin materials, and that cooling is significantly more efficient for atomically thin crystals than for thicker crystals. Importantly, when such thin crystals are placed in air, their overall cooling ability is enhanced by their efficient interaction with air molecules. The mechanism for this is likely the coupling of phonon modes in $MoSe_2$ to various degrees of motion of the surrounding molecules, including their vibrational modes.[43] This is very relevant and beneficial for designing applications where the thermal management of TMDs and other layered materials is a crucial consideration.

3. Conclusion

We used Raman thermometry and ab initio simulations to investigate the influence of thickness on the thermal conductivity of suspended $MoSe_2$ crystals. We observed excellent agreement between our experimentally measured and computed in-plane lattice conductivities. Both approaches indicate a relatively weak effect of crystal thickness on the lattice thermal conductivity κ – within a factor two. We explain this weak thickness influence as the result of competing effects in the phonon contribution to the thermal conductivity. Furthermore, we have demonstrated a very strong effect of the environment on thermal transport, in particular in the case of monolayer $MoSe_2$, which is caused by out-of-plane heat dissipation with a surprisingly large heat transfer coefficient. We note that many of these results represent essential guidance for the thermal investigation of other TMD materials. This work provides a basis to understand and engineer thermal transport properties of a broad class of materials, with promising applications in flexible (opto-)electronic devices.

4. Experimental Section

Sample Fabrication: The sample fabrication, based on PDMS-assisted dry transfer of mechanically exfoliated $MoSe_2$ flakes (HQ graphene, 2H phase), is described in detail elsewhere.[34] As substrates, holey Si_3N_4 membranes (Norcada, NTPR005D-C15) were used for the study of the effect of crystal thickness and the effect of gold coating, (see samples in Figure 1c and Figure S7a, Supporting Information). Those substrates have a single hole with a radius of 7.5 μm. For the study of the effect of hole size, dry-transferred monolayer flakes were used over gold-coated silicon-on-insulator wafers with back-thinned membranes with holes. Focused ion beam was used to perforate holes with a radius of 2.5 and 5 μm prior to transfer (see Figure S7b, Supporting Information). The gold coatings, consisting of 50 nm gold with 5 nm titanium adhesion layer, were deposited prior to transfer using E-beam evaporation (AJA Orion).

Raman Thermometry: Raman spectra were collected with a Horiba T64000 Raman spectrometer and a laser beam, with a wavelength of $\lambda = 532$ nm, focused to a $1/e$ spot size of ≈1 μm (see Figure S15, Supporting Information for spot size measurements). For thermal measurements, the samples were placed in a temperature-controlled vacuum stage (Linkam). The samples were glued onto a holey Cu plate using silver paste, for a good thermal link with the stage. The samples were left to thermalize for 20 min at each temperature. These calibration measurements were taken both in the supported and suspended regions, giving comparable results (see Supporting Information). The temperature increase was defined as $\Delta T = (\nu_P - \nu_{P=0})/\chi_T$, with $\nu_{P=0}$ the intercept from the linear fit of Raman shift with laser

power. The Raman experiments were performed both in vacuum (5×10^{-3} mbar) and air (1 bar). The absorbance of each suspended $MoSe_2$ crystal was determined using a home-built optical setup by measuring transmittance and reflectance through the suspended region, see Supporting Information. For all thicknesses, homogeneous heating in the c-axis of the flake was assumed. The error bars in the experimental thermal conductivity were obtained from the uncertainty in absorption, flake thickness (only for the thicker flakes), and Raman laser spot size, as well as statistical errors in the fitted Raman shifts, accumulating to ≈30% for the thinnest flakes and ≈20% for the thicker flakes. Multiple measurements on different samples with the same thickness, for example, the four bilayer samples, demonstrated that sample-to-sample variations fall within this experimental uncertainty.

Density Functional Theory Simulations: The computational approach was based on first-principles calculations. Thermal transport properties were studied using the density functional theory as implemented in the SIESTA program[31,32] and employing LMKLL functionals[45] to take into account van der Waals interactions. Structures with a different number of layers, from monolayer up to 6L, with 17 Å of vacuum were considered to eliminate the interaction between periodically repeated images.

Calculations were converged with 1000 Ry energy cutoff for the real-space grid with a $(20 \times 20 \times 1)$ **k**-points sampling of the Brillouin zone for all the layers and $(20 \times 20 \times 20)$ **k**-points grid for the bulk. A standard double zeta polarized (DZP) basis for Mo and Se atoms and an electronic temperature of 300 K was used. The conjugate gradient algorithm was used to relax the cell and the atomic positions until the forces on the atoms became smaller than 0.001 eV Å^{-1} and the maximum stress component is smaller than 0.5 GPa.

The calculations of forces and stress were then performed with $(10 \times 10 \times 1)$ supercells and $(8 \times 8 \times 2)$ supercells for the bulk material with the standard diagonalization method. The number of atoms in the supercells varied from 192 atoms in the monolayer to 1152 atoms in the six-layer flake. The thermal properties were then computed with the TDEP method. The convergence of forces in TDEP required seven iterations, where an iteration consisted in generating a set of displacements, computing forces, and fitting force-constants. The temperature used to generate snapshots was varied between 300 and 500 K. To better average the forces, the number of configurations used in the procedure was increased as a geometrical series, with the seventh iteration computed using 128 configurations. The thermal conductivity was calculated by iteratively solving the full Boltzmann transport equation for several **q**-point grid densities and extrapolating the value for an infinite number of **q**-points.

Supporting Information

Supporting Information is available from the Wiley Online Library or from the author.

Acknowledgements

2108352 (8 of 9)

Conflict of Interest

The authors declare no conflict of interest.

Data Availability Statement

The data that support the findings of this study are available from the corresponding author upon reasonable request.

Keywords

[1] Q. H. Wang, K. Kalantar-Zadeh, A. Kis, J. N. Coleman, M. S. Strano, *Nat. Nanotechnol.* **2012**, *7*, 699.

[2] J.-W. T. Seo, J. Zhu, V. K. Sangwan, E. B. Secor, S. G. Wallace, M. C. Hersam, *ACS Appl. Mater. Interfaces* **2019**, *11*, 5675.

[3] S. Manzeli, D. Ovchinnikov, D. Pasquier, O. V. Yazyev, A. Kis, *Nat. Rev. Mater.* **2017**, *2*, 17033.

[4] O. Lopez-Sanchez, D. Lembke, M. Kayci, A. Radenovic, A. Kis, *Nat. Nanotechnol.* **2013**, *8*, 497.

[5] W. Du, P. Yu, J. Zhu, C. Li, H. Xu, J. Zou, C. Wu, Q. Wen, H. Ji, T. Liu, Y. Li, G. Zou, J. Wu, Z. M. Wang, *Nanotechnology* **2020**, *31*, 225201.

[6] T. Roy, M. Tosun, J. S. Kang, A. B. Sachid, S. B. Desai, M. Hettick, C. C. Hu, A. Javey, *ACS Nano* **2014**, *8*, 6259.

[7] H.-J. Chuang, B. Chamlagain, M. Koehler, M. M. Perera, J. Yan, D. Mandrus, D. Tomanek, Z. Zhou, *Nano Lett.* **2016**, *16*, 1896.

[8] S. Yang, C. Jiang, S.-h. Wei, *Appl. Phys. Rev.* **2017**, *4*, 021304.

[9] R. K. Jha, J. V. D'Costa, N. Sakhuja, N. Bhat, *Sens. Actuators, B* **2019**, *297*, 126687.

[10] J. Y. Oh, J. H. Lee, S. W. Han, S. S. Chae, E. J. Bae, Y. H. Kang, W. J. Choi, S. Y. Cho, J.-O. Lee, H. K. Baik, T. I. Lee, *Energy Environ. Sci.* **2016**, *9*, 1696.

[11] K. F. Mak, C. Lee, J. Hone, J. Shan, T. F. Heinz, *Phys. Rev. Lett.* **2010**, *105*, 136805.

[12] A. Ciarrocchi, A. Avsar, D. Ovchinnikov, A. Kis, *Nat. Commun.* **2018**, *9*, 919.

[13] V. Babacic, D. Saleta Reig, S. Varghese, T. Vasileiadis, E. Coy, K.-J. Tielrooij, B. Graczykowski, *Adv. Mater.* **2021**, *33*, 2008614.

[14] B. Huang, G. Clark, E. Navarro-Moratalla, D. R. Klein, R. Cheng, K. L. Seyler, D. Zhong, E. Schmidgall, M. A. McGuire, D. H. Cobden, W. Yao, D. Xiao, P. Jarillo-Herrero, X. Xu, *Nature* **2017**, *546*, 270.

[15] A. A. Balandin, S. Ghosh, W. Bao, I. Calizo, D. Teweldebrhan, F. Miao, C. N. Lau, *Nano Lett.* **2008**, *8*, 902.

[16] Q. Cai, D. Scullion, W. Gan, A. Falin, S. Zhang, K. Watanabe, T. Taniguchi, Y. Chen, E. J. Santos, L. H. Li, *Sci. Adv.* **2019**, *5*, eaav0129.

[17] P. Jiang, X. Qian, X. Gu, R. Yang, *Adv. Mater.* **2017**, *29*, 1701068.

[18] S. E. Kim, F. Mujid, A. Rai, F. Eriksson, J. Suh, P. Poddar, A. Ray, C. Park, E. Fransson, Y. Zhong, D. A. Muller, P. Erhart, D. G. Cahill, J. Park, *Nature* **2021**, *597*, 660.

[19] S. Huberman, R. A. Duncan, K. Chen, B. Song, V. Chiloyan, Z. Ding, A. A. Maznev, G. Chen, K. A. Nelson, *Science* **2019**, *364*, 375.

[20] Y. Zhao, Y. Cai, L. Zhang, B. Li, G. Zhang, J. T. L. Thong, *Adv. Funct. Mater.* **2020**, *30*, 1903929.

[21] H. Zobeiri, R. Wang, T. Wang, H. Lin, C. Deng, X. Wang, *Int. J. Heat Mass Transfer* **2019**, *133*, 1074.

[22] X. Zhang, D. Sun, Y. Li, G.-H. Lee, X. Cui, D. Chenet, Y. You, T. F. Heinz, J. C. Hone, *ACS Appl. Mater. Interfaces* **2015**, *7*, 25923.

[23] E. Easy, Y. Gao, Y. Wang, D. Yan, S. M. Goushehgir, E.-H. Yang, B. Xu, X. Zhang, *ACS Appl. Mater. Interfaces* **2021**, *13*, 13063.

[24] J. J. Bae, H. Y. Jeong, G. H. Han, J. Kim, H. Kim, M. S. Kim, B. H. Moon, S. C. Lim, Y. H. Lee, *Nanoscale* **2017**, *9*, 2541.

[25] P. Yuan, R. Wang, T. Wang, X. Wang, Y. Xie, *Phys. Chem. Chem. Phys.* **2018**, *20*, 25752.

[26] B. Peng, H. Zhang, H. Shao, Y. Xu, X. Zhang, H. Zhu, *RSC Adv.* **2016**, *6*, 5767.

[27] X. Gu, R. Yang, *Appl. Phys. Lett.* **2014**, *105*, 131903.

[28] S. Chen, A. L. Moore, W. Cai, J. W. Suk, J. An, C. Mishra, C. Amos, C. W. Magnuson, J. Kang, L. Shi, R. S. Ruof, *ACS Nano* **2011**, *5*, 321.

[29] X. Gu, B. Li, R. Yang, *J. Appl. Phys.* **2016**, *119*, 085106.

[30] A. J. Gabourie, S. V. Suryavanshi, A. B. Farimani, E. Pop, *2D Mater.* **2020**, *8*, 011001.

[31] J. M. Soler, E. Artacho, J. D. Gale, A. García, J. Junquera, P. Ordejón, D. Sánchez-Portal, *J. Phys.: Condens. Matter* **2002**, *14*, 2745.

[32] A. García, N. Papior, A. Akhtar, E. Artacho, V. Blum, E. Bosoni, P. Brandimarte, M. Brandbyge, J. I. Cerdá, F. Corsetti, R. Cuadrado, V. Dikan, J. Ferrer, J. Gale, P. García-Fernández, V. M. García-Suárez, S. García, S. Huhs, S. Illera, R. Korytár, P. Koval, I. Lebedeva, L. Lin, P. López-Tarifa, S. G. Mayo, S. Mohr, P. Ordejón, A. Postnikov, Y. Pouillon, M. Pruneda, R. Robles, D. Sánchez-Portal, J. M. Soler, R. I. Ullah, V. Wen-zhe Yu, J. Junquera, *J. Chem. Phys.* **2020**, *152*, 204108.

[33] E. Chávez-Ángel, J. S. Reparaz, J. Gomis-Bresco, M. R. Wagner, J. Cuffe, B. Graczykowski, A. Shchepetov, H. Jiang, M. Prunnila, J. Ahopelto, F. Alzina, C. M. Sotomayor Torres, *APL Mater.* **2014**, *2*, 012113.

[34] S. Varghese, D. Saleta Reig, J. D. Mehew, A. Block, A. E. Sachat, E. Chávez-Ángel, M. Sledzinska, B. Ballesteros, C. M. Sotomayor Torres, K.-J. Tielrooij, *J. Phys.: Mater.* **2021**, *4*, 046001.

[35] W. Cai, A. L. Moore, Y. Zhu, X. Li, S. Chen, L. Shi, R. S. Ruoff, *Nano Lett.* **2010**, *10*, 1645.

[36] R. Wang, T. Wang, H. Zobeiri, P. Yuan, C. Deng, Y. Yue, S. Xu, X. Wang, *Nanoscale* **2018**, *10*, 23087.

[37] O. Hellman, I. A. Abrikosov, S. I. Simak, *Phys. Rev. B* **2011**, *84*, 180301.

[38] O. Hellman, P. Steneteg, I. A. Abrikosov, S. I. Simak, *Phys. Rev. B* **2013**, *87*, 104111.

[39] S. Ghosh, W. Bao, D. L. Nika, S. Subrina, E. P. Pokatilov, C. N. Lau, A. A. Balandin, *Nat. Mater.* **2010**, *9*, 555.

[40] S. Kumar, U. Schwingenschlögl, *Chem. Mater.* **2015**, *27*, 1278.

[41] A. Kandemir, H. Yapicioglu, A. Kinaci, T. Çağın, C. Sevik, *Nanotechnology* **2016**, *27*, 055703.

[42] T. L. Bergman, F. P. Incropera, D. P. DeWitt, A. S. Lavine, *Fundamentals of Heat and Mass Transfer*, Wiley, New York **2011**.

[43] D. Mann, E. Pop, J. Cao, Q. Wang, K. Goodson, H. Dai, *J. Phys. Chem. B* **2006**, *110*, 1502.

[44] A. R. Beal, H. P. Hughes, *J. Phys. C: Solid State Phys.* **1979**, *12*, 881.

[45] K. Lee, É. D. Murray, L. Kong, B. I. Lundqvist, D. C. Langreth, *Phys. Rev. B* **2010**, *82*, 081101.